J. Synchrotron Rad. (2000). **7**, 296–300

First results from the Canadian SGM beamline at SRC

B. W. Yates,[a] Y. F. Hu,[b]* K. H. Tan,[a] G. Retzlaff,[a] R. G. Cavell,[c] T. K. Sham[b] and G. M. Bancroft[b]

[a]Canadian Synchrotron Radiation Facility (CSRF), University of Wisconsin-Madison, Stoughton, WI 53589, USA, [b]Department of Chemistry, The University of Western Ontario, London, Ontario N6A 5B7, Canada, and [c]Department of Chemistry, University of Alberta, Edmonton, AB T6G 2G2, Canada. E-mail: yhu@julian.uwo.ca

(*Received 22 March 2000; accepted 11 May 2000*)

The first experimental results obtained from the Canadian SGM beamline at SRC (Synchrotron Radiation Centre, University of Wisconsin-Madison, USA) are reported. The beamline is based on the Dragon-type design, with a constant deviation angle, using photons from a second-generation bending-magnet light source. The medium-energy grating on this beamline covers a photon energy range from 240 to 700 eV, with a ruling density of 600 lines mm^{-1}. A maximum resolving power of ~10000 is achieved at a photon energy of ~400 eV. Gas-phase absorption spectra collected at the N, O and C *K*-edges are presented to demonstrate the excellent performance of this beamline. High-resolution absorption spectra of some C- and Ti-containing solid-state samples are also reported.

Keywords: spherical-grating monochromators; soft X-rays; bending-magnet radiation; absorption spectroscopy; vibrational fine structure.

1. Introduction

Over the last decade, grazing-incidence-type monochromators, such as the spherical-grating monochromator (SGM) (Chen, 1987) and plane-grating monochromator (PGM) (Petersen, 1982), have been developed as the primary high-resolution/flux monochromators in the soft X-ray region (100–1000 eV). Two types of SGMs have been designed and are in full operation. The first type is of the original Dragon design, *i.e.* an SGM that is operated with a constant deviation angle by scanning the entrance and/or exit slits (Chen & Sette, 1989). The second type is the constant-length Rowland SGM, with an additional plane mirror, that is operated at variable deviation angles (Senf *et al.*, 1992). A resolving power ($E/\Delta E$) of >10000 has been recently reported for both types of SGMs (Dragon type: Quaresima *et al.*, 1995; Shigemasa *et al.*, 1998; constant-length type: Schwarzkopf *et al.*, 1998; Prince *et al.*, 1998). Most of these beamlines are connected to an undulator radiation source from a third-generation storage ring.

In this paper we report the first results obtained from the Canadian Dragon-type SGM beamline located at SRC, University of Wisconsin-Madison, USA. We show that a resolving power of ~10000 and a photon flux of 10^{10} photons s^{-1} can be achieved using a second-generation bending-magnet light source, with full illumination of the grating. We report the high-resolution photoabsorption spectra of gas samples, *e.g.* N_2, NO and CO, and of solid samples, *e.g.* diamond, graphite and TiO_2, to demonstrate the good performance of this beamline.

2. Description of the beamline

A schematic layout of the beamline is shown in Fig. 1. This beamline is connected to Port 063 of SRC. The beamline components were designed and manufactured by McPherson Inc. Optical ray-tracing of this beamline was performed by CSRF staff using the program *SHADOW* (CNTech, Stoughton, WI, USA), and cross-checked with *BEAM IV* (Stellar Software, Berkeley, CA, USA) results from McPherson. Beamline installation and alignment were performed by CSRF/McPherson staff.

A water-cooled aperture is located downstream of the SRC front end, to reduce the beam divergence to 10 mrad (horizontal) × 3 mrad (vertical). The cylindrical mirror M_1 acts as a collimator in the horizontal direction, keeping the

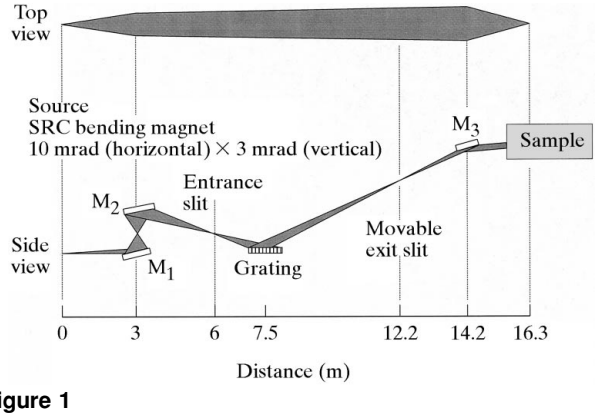

Figure 1
Schematic layout of the Canadian SGM beamline.

Table 1
Parameters of the optical elements.

Optical element	M_1	M_2	Grating	M_3
Shape	Cylinder	Sphere	Sphere	Toroid
Blank material	Glidcop	Glidcop	Fused silica	Fused silica
Coating	250 Å gold	250 Å gold	2000 Å gold	250 Å gold
Surface roughness (r.m.s.) (Å)	20	20	10	20
Slope error (r.m.s.) (arcsec)	2	2	0.2	2/10
Radius (m)	0.18182	86.32	70.477†	59.314/0.141
Ruling density (lines mm^{-1})			600†	
Included angle (°)	176	176	175	176
Optical surface [length (mm) × width (mm)]	300 × 50	300 × 50	210 × 40	160 × 40

† Medium-energy grating.

photon beam at ~2.5 cm in horizontal width until reaching the refocusing mirror M_3. The spherical mirror M_2, just downstream, focuses the light vertically onto the entrance slit (vertical full width at half-maximum $\simeq$ 250 μm) using 1:1 magnification. Both mirrors are gold-coated and designed for 2° grazing operation. The spherical grating (gold-coated) disperses the light into the required wavelength using inside order, onto a movable exit slit. The exit slit is set so that the defocus term is zero. The monochromator is designed for a constant included angle of 175°, which results in the exit slit being on a 5° slope from the horizontal. After a 2° grazing-incidence reflection downwards off the gold-coated toroidal mirror M_3, the light collapses both horizontally and vertically to the experiment focus of ~1 mm × 1 mm. Downstream of the experimental focus, the photon beam rises at 1° from the horizontal.

The surfaces of all the optics were checked by long-trace surface profilometer measurements, performed by Peter Takacs at Brookhaven National Laboratory. The properties of the optical elements are shown in Table 1. The grating was manufactured by Hyperfine, and is an original, ruled in gold with a ruling engine. The grating chamber is designed to hold three gratings; namely a low-, medium- and high-energy grating, to cover the soft X-ray energy range 100–1200 eV. Currently only the medium-energy grating is installed, providing photons from 240 to 700 eV. Entrance and exit slits are made of molybdenum, and can be set over the range 8–1000 μm. The exit slit has a movable range of ±350 mm, under computer control *via* a stepping motor. The entrance slit has a much smaller range of ±50 mm *via* a hand crank, which can be used to tweak the entrance-slit position to obtain optimal resolution. Normally the entrance slit is fixed in position at this optimal setting.

Downstream from the M_3 refocusing mirror, just prior to the experimental focus, a differential pumping section made by X-ray Instrumentation Associates is installed. This differential pumping section effectively isolates the refocusing mirror from the user experimental station. Two Ni grids (90% transmitting) are installed just downstream of the differential pumping section, to monitor the I_0 signal required for intensity normalization. A 1500 Å-thick carbon or aluminium window from Luxel (supported on 80% transmitting Ni mesh) is installed downstream from the I_0 monitor. The I_0 signal, as well as the photoabsorption electron yields reported in this work, are measured using Keithley 617 electrometers, and read *via* computer through a GPIB connection. A calibrated silicon photodiode from International Radiation Detectors (model AXUV-100) is used to measure the absolute photon flux. Fig. 2 shows the normalized photon flux of the Canadian SGM beamline measured at the end of the photoionization gas cell. The reported photon flux has been corrected for the transmission of the Ni grids and the 1500 Å-thick carbon window. A maximum flux of 1.6×10^{10} photon s^{-1} (normalized to a ring current of 100 mA, and a 100 μm setting for both entrance and exit slits) is observed at a photon energy of ~330 eV. This flux compares very favourably with the reported fluxes from the other second-generation ring-based SGM beamlines (Hussain *et al.*, 1996; Schwarzkopf *et al.*, 1998). It is estimated that the contribution due to the second order of the grating is about 16% near the C *K*-edge (290 eV). The medium-energy grating for this beamline covers the *K*-edges of carbon, nitrogen and oxygen, as well as the *L* and *M* edges of numerous second-row transition metals. It is important to note that the photon flux shown in Fig. 2 indicates that the Canadian SGM beamline is relatively free of contamination by most of the above-

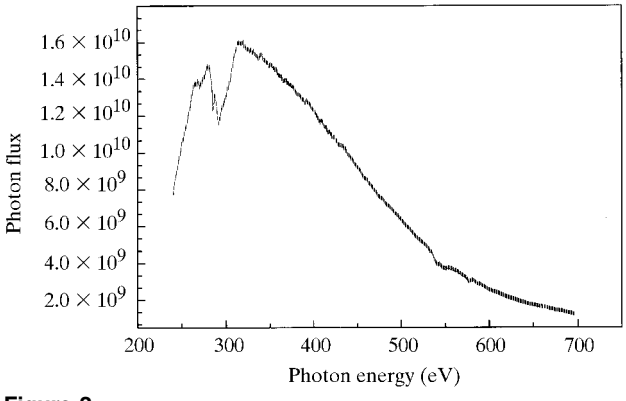

Figure 2
Absolute photon flux measured at the end of the Canadian SGM beamline. The structure around 300 eV is due to the carbon contamination of the optical surfaces. The flux is normalized to a ring current of 100 mA and a 100 μm slit setting for both entrance and exit slits. Units of photon flux on the *y*-axis are photons s^{-1} (100 mA beam)$^{-1}$ (100 μm × 100 μm)$^{-1}$.

mentioned elements, with the exception of C. This makes it relatively simple to perform background normalization for photoabsorption measurements.

A monochromator-control/data-acquisition program has been written in *Labview* (National Instruments, Austin, TX, USA) for the Canadian SGM beamline. Two different scanning modes are available, to control motions of the stepper motors that are connected to the exit slit and to the grating through a sine drive mechanism. 'Fixed focus' mode scans both the grating and the exit slit simultaneously, for optimal resolution results. The exit slit is set in this mode so that the defocus term is zero. 'Wavelength' mode, on the other hand, scans the grating mechanism for wavelength, but leaves the exit slit fixed at a position that is selected by the user. This mode is typically chosen for a scan over a small photon energy range, where ultimate resolution is not the major concern. The experimental results shown in this paper were collected entirely in 'fixed focus' mode.

Two different end-station measurements will be reported in this paper. A double ionization gas cell (10 cm active pathlength in each chamber) was used for the gas-phase photoabsorption measurements. Typical gas pressures of <25 mtorr were used in the gas cell, as measured by a temperature-regulated MKS baratron (1 torr head). The gas samples reported in this work were all commercially available (research grade) and used without further purification. Typical photoionization currents in the range 1–10 pA were measured. A 10 μm slit setting for both entrance and exit slits was used for all the gas-phase measurements reported in this work. A solid-state chamber was used to obtain the near-edge absorption fine-structure (NEXAFS) spectra for the solids. This chamber is capable of simultaneously measuring both total electron yield (TEY) and fluorescence yield (FY) on solid samples. A 50 μm slit setting for both entrance and exit slits was used for the solid-state measurements reported in §3.2.

3. Results and discussion

3.1. *Gas-phase results*

The *K*-edge photoabsorption spectrum of gas-phase nitrogen is normally used as the benchmark test for the monochromator resolution in the soft X-ray region. A series of vibrational states (up to seven or eight) can be resolved for the N $1s \rightarrow \pi_g^*$ transition at high resolution. The monochromator resolution can be extracted by fitting the resolved vibrational peaks to a series of Voigt functions. The Gaussian component is generally taken as the instrumental resolution (Prince *et al.*, 1999). The N_2 NEXAFS spectrum obtained using first-order light from the Canadian SGM beamline is shown in Fig. 3. This spectrum was measured in 'fixed focus' mode with an 8 μm entrance/exit-slit setting, 10 mtorr pressure and full illumination of the grating. Seven Voigt peaks were fitted to this spectrum. The Lorentzian width was fixed at 115 meV, taken from the most recent literature value of N $1s_g^{-1}\pi^*$ lifetime broadening (Prince *et al.*, 1999). This yields a Gaussian width of 38.4 ± 2 meV (and a total peak width of 132 meV), and a resolving power of ~10000 at 400 eV for our beamline. One should note that there is some uncertainty in the estimation of the resolving power, owing to the error in the fitting routine and overestimation of the Lorentzian width (Vondracek *et al.*, 1999). The achieved resolving power of this beamline exceeds our design goal of 5000 and is very comparable with the highest resolving power reported from the other third-generation undulator-based SGM beamlines (Prince *et al.*, 1998; Schwarzkopf *et al.*, 1998).

As a result of the good beamline performance at a photon energy of ~400 eV, we are now able to obtain the high-resolution N *K*-edge spectrum of more complicated N-containing molecules, such as the diatomic open-shell molecule nitric oxide (NO). When one of the N 1*s* electrons in NO is photoexcited into the empty π^* orbital, this excited electron will interact with the single π^* electron in the electronic ground state, leading to three observable electronic states, namely the $^2\Delta$, $^2\Sigma^-$ and $^2\Sigma^+$ states. These states have been observed with modest resolution in the N *K*-edge spectrum of NO (Ma *et al.*, 1991; Remmers *et al.*, 1993). The NEXAFS spectrum of NO, representing the N $1s^2\pi^* \rightarrow 1s(\pi^*)^2$ transition, is shown in Fig. 4. Compared with the previously published spectra (Ma *et al.*, 1991; Kosugi *et al.*, 1992; Remmers *et al.*, 1993), the vibrational fine structure associated with the $^2\Delta$, $^2\Sigma^-$ and $^2\Sigma^+$ states are much better resolved in Fig. 4. For example, the shoulder at ~399.6 eV is clearly visible in Fig. 4, but not resolved in the previous studies (Ma *et al.*, 1991; Kosugi *et al.*, 1992; Remmers *et al.*, 1993). The spectrum was fit into a series of vibrational peaks with Voigt profiles. The vibrational states were described by applying an algorithm, which performed a Franck–Condon analysis to calculate the vibrational substates (Püttner *et al.*, 1999). Our fitting results indicate a longer equilibrium distance (from 1.15 Å to 1.22 Å) and a lower vibrational energy (from 236 meV to 204 meV) for the core excited states compared with the

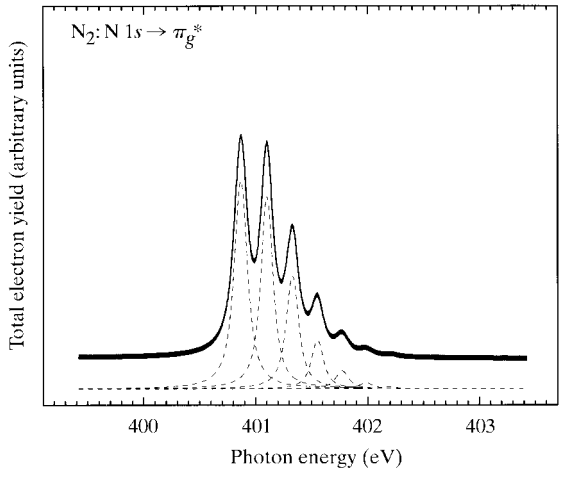

Figure 3
N $1s \rightarrow 1\pi_g^*$ photoabsorption spectrum of gas-phase N_2, recorded in total electron yield.

ground state. This implies a weakening of the molecular bond upon N 1*s* core ionization of NO, in agreement with the bond weakening reported recently in the high-resolution O *K*-edge spectrum of NO (Püttner *et al.*, 1999).

The NEXAFS spectra of CO gas, representing the C $1s \rightarrow 2\pi^*$ and O $1s \rightarrow 2\pi^*$ transitions, are presented in Fig. 5. Four vibrational states are resolved in the C $1s^{-1}2\pi^*$ spectrum shown in Fig. 5(*a*). Prince and co-workers have recently reported a better C $1s^{-1}2\pi^*$ spectrum of CO, where five vibrational states were resolved (Prince *et al.*, 1999). However, our C $1s^{-1}2\pi^*$ spectrum is certainly better resolved than the C $1s^{-1}2\pi^*$ spectra reported earlier (Ma *et al.*, 1991; Domke *et al.*, 1990). Our least-squares fit of Fig. 5(*a*) indicates an instrumental contribution of 52 $\pm$ 2 meV, assuming a lifetime broadening of 79 meV (Prince *et al.*, 1999). This yields a resolving power of 5500 for our monochromator at the carbon *K*-edge. Extensive vibrational fine structure is clearly resolved in the O $1s^{-1}2\pi^*$ spectrum of CO shown in Fig. 5(*b*). The quality of this spectrum is close to that of the best spectra reported so far in the literature (Coreno *et al.*, 1999; Püttner *et al.*, 1999). However, this spectrum is certainly better resolved than the spectrum reported much earlier by Domke and co-workers (Domke *et al.*, 1990). The least-squares fit of Fig. 5(*b*) yields a Gaussian width of 108 $\pm$ 4 meV, assuming a lifetime broadening of 160 meV (Prince *et al.*, 1999; Coreno *et al.*, 1999). Thus, a resolving power of close to 5000 is estimated for our beamline at the oxygen *K*-edge.

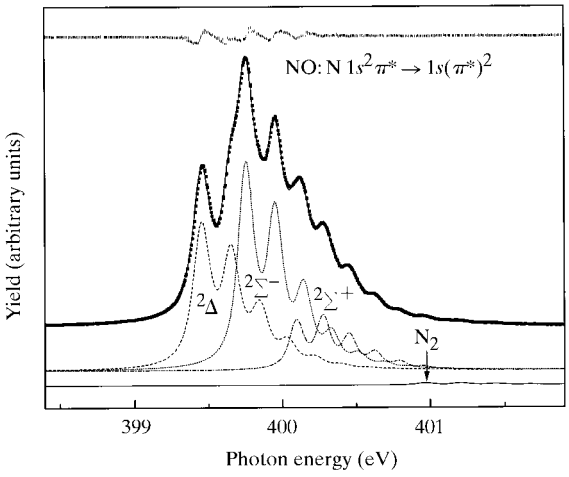

Figure 4
N $1s^2\pi^* \rightarrow 1s(\pi^*)^2$ photoabsorption spectrum of NO. A contribution of about 1–2% from N_2 gas is included in the fitted spectrum. This small amount of N_2 impurity is probably due to the photodissociation of NO by the soft X-ray light (Püttner *et al.*, 1999).

3.2. *Solid-state results*

The Canadian SGM beamline was also designed for high-resolution photoemission and X-ray absorption spectroscopy of solid-state materials and surfaces. Fig. 6 shows the C *K*-edge NEXAFS spectra of three different carbon samples recorded in total electron yield (TEY). The edge features for diamond and for graphite ($1s \rightarrow \pi^*$ and $1s \rightarrow$

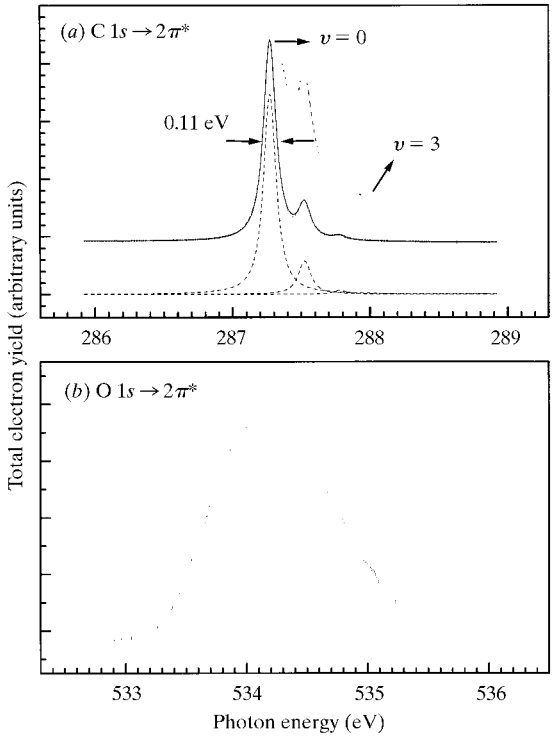

Figure 5
(*a*) C $1s \rightarrow 2\pi^*$ and (*b*) O $1s \rightarrow 2\pi^*$ photoabsorption spectra of CO.

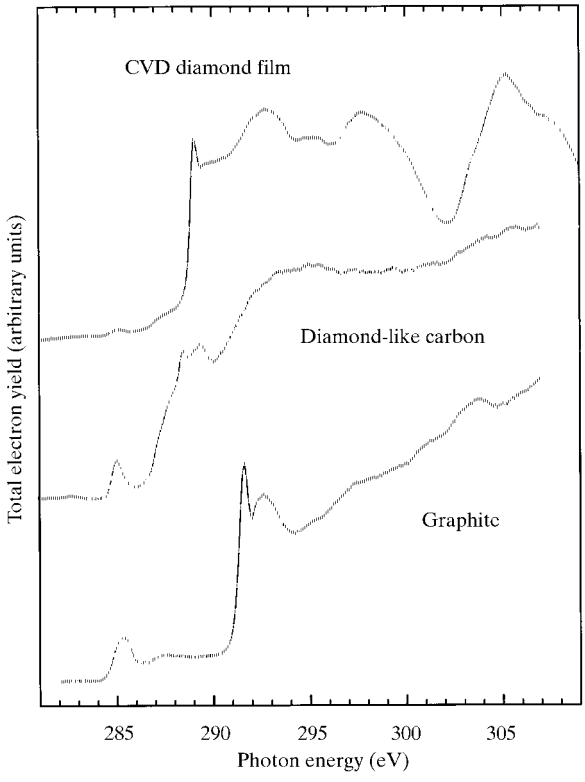

Figure 6
C *K*-edge photoabsorption spectra of diamond, diamond-like carbon and graphite.

σ^* transitions) are much sharper than the spectra reported recently for these materials (García *et al.*, 1998; Gouzman *et al.*, 1999). The very distinctive features for sp^2-bonded graphite and sp^3-bonded diamond are well resolved, while the diamond film treated by chemical vapour deposition (CVD) exhibits primarily diamond-like bonding, with some graphite features. More details of this work will be published elsewhere (Sham & Lifshitz, 2000).

Fig. 7 presents Ti $L_{2,3}$-edge NEXAFS spectra of two Ti solid-state samples. The TEY spectrum of TiO_2 (rutile) is in good agreement with the published high-resolution NEXAFS spectrum (van der Laan, 1990). The additional splitting of the Ti 2*p* spin–orbit peaks can be explained by crystal field splitting of the excited Ti 3*d* orbitals (van der Laan, 1990). The TEY spectrum of an evaporated Ti film on an Si(100) wafer is remarkably similar to the TiO_2 spectrum. Since this spectrum was measured in TEY mode at a surface-sensitive grazing-incidence angle, this indicates that the Ti metal at the surface of the silicon wafer has been heavily oxidized to form TiO_2. It is only when bulk-sensitive fluorescence yield (FY) measurements are made at normal incidence on this sample that the chemically shifted features corresponding to Ti metal become distinctive at lower binding energy.

4. Summary

Our results show that the Canadian SGM beamline delivers high resolution over a wide photon energy range. It has reasonably good photon flux, using photons from a second-generation bending-magnet source. A high-performance photoemission spectrometer and two additional gratings are to be installed in the near future. This should enable users to perform both high-resolution photoabsorption and photoemission measurements over the full soft X-ray region.

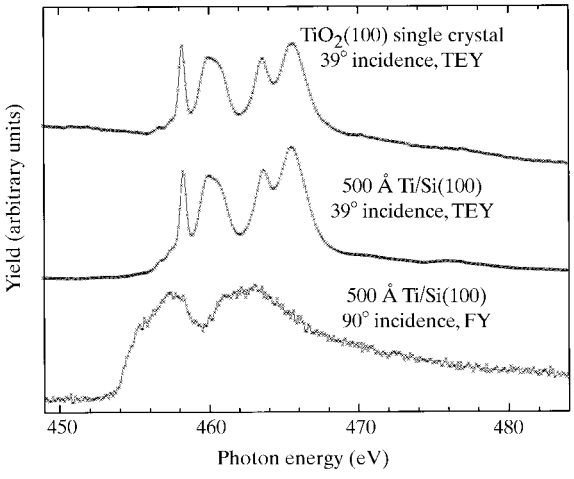

Figure 7
Ti $L_{2,3}$-edge photoabsorption spectra of TiO_2 (rutile), recorded in total electron yield, and of 500 Å Ti/Si(100), recorded both in total electron and fluorescence yields.

We acknowledge financial support from the Natural Sciences and Engineering Research Council (NSERC) of Canada for this work. We are grateful to the staff, especially Dan Wallace and Greg Rogers of SRC, for their technical assistance. The Synchrotron Radiation Centre of the University of Wisconsin is supported by the National Science Foundation under Grant No. DMR-95-31009. We thank Dr R. Püttner for his help in fitting the NO spectrum. We thank Dr Y. Lifshitz for providing the CVD diamond and diamond-like carbon samples.

References

Chen, C. T. (1987). *Nucl. Instrum. Methods A*, **256**, 595–604.
Chen, C. T. & Sette, F. (1989). *Rev. Sci. Instrum.* **60**, 1616–1621.
Coreno, M., de Simone, M., Prince, K. C., Richter, R., Vondracek, M., Avaldi, L. & Camilloni, R. (1999). *Chem. Phys. Lett.* **306**, 269–274.
Domke, M., Xue, C., Puschmann, A., Mandel, T., Hudson, E., Shirley, D. A. & Kaindl, G. (1990). *Chem. Phys. Lett.* **173**, 122–128.
García, M. M., Jiménez, I., Vázquez, L., Gómez-Aleixandre, C., Albella, J. M., Sáchez, O., Terminello, L. J. & Himpsel, F. J. (1998). *Appl. Phys. Lett.* **72**, 2105–2107.
Gouzman, I., Shima-Edelstein, R., Comtet, G., Hellner, L., Dujardin, G., Roter, S. & Hoffman, A. (1999). *Diamond Relat. Mater.* **8**, 132–138.
Hussain, Z., Huff, W. R. A., Kellar, S. A., Moler, E. J., Heimann, P. A., McKinney, W., Padmore, H. A., Fadley, C. S. & Shirley, D. A. (1996). *J. Electron Spectrosc. Relat. Phenom.* **80**, 401–404.
Kosugi, N., Adachi, A., Shigemasa, E. & Yagishita, A. (1992). *J. Chem. Phys.* **97**, 8842–8849.
Laan, G. van der (1990). *Phys. Rev. B*, **41**, 12366–12368.
Ma, Y., Chen, C. T., Meigs, G., Randall, K. & Sette, F. (1991). *Phys. Rev. A*, **44**, 1848–1858.
Petersen, H. (1982). *Opt. Commun.* **40**, 402–406.
Prince, K. C., Blyth, R. R., Delaunay, R., Zitnik, M., Krempasky, J., Slezak, J., Camilloni, R., Avaldi, L., Coreno, M., Stefani, G., Furlani, C., de Simone, M. & Stranges, S. (1998). *J. Synchrotron Rad.* **5**, 565–568.
Prince, K. C., Vondracek, M., Karvonen, J., Coreno, M., Camilloni, R., Avaldi, L. & de Simone, M. (1999). *J. Electron Spectrosc. Relat. Phenom.* **103**, 141–147.
Püttner, R., Dominguez, I., Morgan, T. J., Cisneros, C., Fink, R. F., Rotenberg, E., Warwick, T., Domke, M., Kaindl, G. & Schlachter, A. S. (1999). *Phys. Rev. A*, **59**, 3415–3423.
Quaresima, C., Ottaviani, C., Matteucci, M., Crotti, C., Antonini, A., Capozi, M., Rinaldi, S., Luce, M., Perfetti, P., Prince, K. C., Astaldi, C., Zacchigna, M., Romanzin, L. & Savoia, A. (1995). *Nucl. Instrum. Methods A*, **364**, 374–379.
Remmers, G., Domke, M., Puschmann, A., Mandel, T. & Kaindl, G. (1993). *Chem. Phys. Lett.* **214**, 241–249.
Schwarzkopf, O., Eggenstein, F., Flechsig, U., Kalus, C., Lammert, H., Menthel, U., Reichardt, G., Rotter, P., Senf, F., Zeschke, T. & Peatman, W. B. (1998). *Rev. Sci. Instrum.* **69**, 3789–3793.
Senf, F., Eggenstein, F. & Peatman, W. (1992). *Rev. Sci. Instrum.* **63**, 1326–1329.
Sham, T. K. & Lifshitz, Y. (2000). Personal communication.
Shigemasa, E., Toyoshima, A., Yan, Y., Hayaishi, T., Soejima, K., Kiyokura, T. & Yagishita, A. (1998). *J. Synchrotron Rad.* **5**, 777–779.
Vondracek, M., Prince, K. C., Karvonen, J., Coreno, M., Camilloni, R., Avaldi, L. & de Simone, M. (1999). *Synchrotron Rad. News*, **12**, 27–30.